Nano Research

Open Access

Research Article

Mechanism of influence of solvent types and Sn valence states on performance of $Cu_2ZnSn(S, Se)_4$ solar cell

Mengge Li[1,2], Bin Yao[1,2]✉, Yongfeng Li[1,2]✉, Zhanhui Ding[1,2], Shuang Li[1,2], Hongmei Luan[3], Ning Ding[1,2], and Liyuan Shi[1,2]

[1] *State Key Laboratory of High Pressure and Superhard Materials, College of Physics, Jilin University, Changchun 130012, China*
[2] *Key Laboratory of Physics and Technology for Advanced Batteries (Ministry of Education), College of Physics, Jilin University, Changchun 130012, China*
[3] *School of Physical Science and Technology, Inner Mongolia University, Hohhot 010021, China*

Cite this article: *Nano Research*, **2026**, *19*, 94908700. https://doi.org/10.26599/NR.2026.94908700

ABSTRACT: In the present work, two types of $Cu_2ZnSn(S, Se)_4$ (CZTSSe) solar cells, namely cell-MOE (MOE refers to 2-methoxyethanol) and cell-DMSO (DMSO refers to dimethyl sulfoxide), were fabricated using two Cu_2ZnSnS_4 (CZTS) precursor solutions: one employing MOE solvent and Sn^{4+} salt (MOE-Sn^{4+}), and the other using DMSO solvent and Sn^{2+} (DMSO-Sn^{2+}). Effects of the solvent types and the valence state of Sn on power conversion efficiency (PCE) of CZTSSe solar cell were investigated. It is found that the PCE of CZTSSe solar cells prepared with solution MOE-Sn^{4+} is higher than that of those prepared with solution DMSO-Sn^{2+}. The highest PCE reaches 10.17% for cell-DMSO and 11.25% for cell-MOE. The advantage of MOE-Sn^{4+} solution is attributed to the fact that CZTS precursor film prepared with MOE-Sn^{4+} (CZTS-MOE) possesses a looser crystal structure and smaller grain size than that prepared with DMSO-Sn^{2+} (CZTS-DMSO). These structural and grain characteristics enable the CZTSSe derived from the selenization of CZTS-MOE (CZTSSe-MOE) to exhibit superior crystallinity compared with the CZTSSe obtained via the selenization of CZTS-DMSO (CZTSSe-DMSO). This enables CZTSSe-MOE to have a lower hole concentration, fewer band tail states, lower bulk and surface deep-level defect densities, and a reduced content of the Zn(S, Se) compared with CZTSSe-DMSO. These characteristics in turn endow cell-MOE with a wider depletion region width, stronger light absorption capacity, and less carrier recombination than cell-DMSO, thereby contributing to a higher photogenerated current density and a lower reverse saturation current density in cell-MOE relative to cell-DMSO.

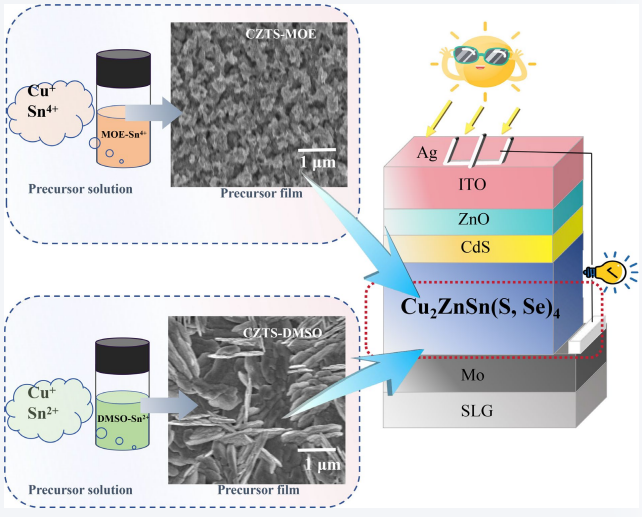

KEYWORDS: $Cu_2ZnSn(S, Se)_4$, solar cells, dimethyl sulfoxide (DMSO)-Sn^{2+}, 2-methoxyethanol (MOE)-Sn^{4+}, recombination

1 Introduction

$Cu_2ZnSn(S, Se)_4$ (CZTSSe) thin film is recognized as an ideal absorber material for fabricating thin-film solar cells owing to its superior properties, including high light absorption coefficient, low manufacturing cost, and environmental benignity [1–5]. In recent years, significant progress has been made in the research on CZTSSe solar cells, and the highest power conversion efficiency (PCE) reached 16.6% to date [6]. However, this PCE is still much lower than the highest PCE of $CuInGaSe_2$ solar cell [7]. The primary critical issue limiting the PCE remains the crystalline quality of both the surface and bulk phases of the CZTSSe thin film. In order to obtain CZTSSe film with high crystal quality, many techniques have been used to prepare CZTSSe films, such as, sol–gel [8–11], the vacuum depositions (vacuum evaporation deposition and vacuum sputtering deposition) [12–14], and

Received: January 10, 2026; **Revised:** March 4, 2026
Accepted: April 1, 2026

✉Address correspondence to Bin Yao, binyao@jlu.edu.cn; Yongfeng Li, liyongfeng@jlu.edu.cn

electrodeposition technologies etc. Among these techniques, the sol–gel technique has become the most commonly used method at present, owing to its simple process, low cost, and the high crystalline quality of the CZTSSe thin films fabricated by it [15–17]. The evolution of the reaction pathway is tightly correlated with the valence states of Cu, Zn, and Sn in metal salts and the types of solvents.

In recent years, research has mainly been carried out using monovalent or divalent Cu salts as the Cu source, divalent or tetravalent Sn salts as the Sn source, divalent Zn salts as the Zn source, and dimethyl sulfoxide (DMSO) and 2-methoxyethanol (MOE) as solvents. Pan and co-workers have investigated effects of valence state of Cu on reaction pathway and crystal quality of CZTSSe [18]. In their study, solutions of monovalent and divalent Cu salts were prepared using DMSO as the solvent. The results showed that the crystal quality of CZTSSe film prepared by selenization of Cu^{+} film is better than that prepared by selenization of Cu^{2+} film, which is attributed by Pan and co-workers to the fact that Cu^{2+} film contains SnS. Xin and co-workers used DMSO as the solvent to study the effect of Sn valence on CZTSSe crystal quality [19]. The crystalline quality of the CZTSSe film prepared by selenizing the Sn^{2+} film is inferior to that prepared by selenizing the Sn^{4+} film, which is attributed by Xin and co-workers to the presence of secondary phases, including SnS, in the Sn^{2+} film. This result differs from that reported by Pan and co-workers, implying that the effects of the valence states and species of the three metals on the crystalline quality of CZTSSe films, especially on the photovoltaic performance of CZTSSe solar cells, need to be further studied.

Besides the valence states the three metals (Cu, Sn, and Zn) and species of the three metals' salts, the solvent is also a critical factor for preparing high-crystalline-quality CZTSSe films. However, to our knowledge, comparative studies on the effects of solvents on CZTSSe films and the photovoltaic performance of CZTSSe solar cells have rarely been reported. In the aforementioned studies by Pan and Xin, both research groups used DMSO to prepare Cu_2ZnSnS_4 (CZTS) precursor solutions and comparatively investigated the effects of the valence states of Cu and Sn on the crystalline quality of CZTSSe, while the solvent type was not varied [18, 19]. In current research on CZTSSe solar cells, the highest cell efficiency has been achieved using MOE as the solvent. Solvents can create different environments during the preparation of precursor solutions. At present, the theoretical mechanism behind the use of different solvent systems and metal salts with different valences is not well understood, so further exploration is still needed.

Recent research demonstrates that MOE is a good solvent used for preparation of CZTS precursor solutions [20–23]. In this work, two precursor solutions were prepared: one using monovalent Cu salts and divalent Zn and Sn salts with DMSO as the solvent, denoted as DMSO-Sn^{2+}, and the other using monovalent Cu salts, divalent Zn salts, and tetravalent Sn salts with MOE as the solvent, denoted as MOE-Sn^{4+}. It is found that the CZTSSe solar cell prepared with MOE-Sn^{4+} (denoted as cell-MOE) possesses higher PCE than the CZTSSe solar cell prepared with DMSO-Sn^{2+} (cell-DMSO). The enhancement mechanism of the PCE regulated by Sn valence states and solvents was investigated via two steps: First, calculating the percentage contribution of electrical parameter variations from cell-DMSO to cell-MOE to the PCE improvement; second, clarifying the correlation between such electrical parameter variations and the differences in the quality and properties of CZTSSe films, as well as device interfaces between the two solar cells.

2 Results and discussion

2.1 Performance of cell-MOE and cell-DMSO solar cells

Two kinds of CZTS precursor solution were prepared by using CuCl, $SnCl_2{\cdot}2H_2O$, $ZnCl_2$, thiourea ($SC(NH_2)_2$), and DMSO, respectively, as well as CuCl, $SnCl_4{\cdot}5H_2O$, $Zn(CH_3COO)_2$, $SC(NH_2)$, and MOE, respectively. The valence states of Cu and Zn, as well as S source, are same in both precursor solutions, but solvent types and valence state of Sn are different. The precursor solution prepared with MOE and Sn^{4+} ions is denoted as MOE-Sn^{4+}, and precursor solution prepared with DMSO and Sn^{2+} ions is denoted as DMSO-Sn^{2+}. In both precursor solutions, Cu/(Zn + Sn) and Zn/Sn atomic ratios are 0.75 and 1.12, respectively. Two kinds of CZTS precursor film, denoted as CZTS-MOE and CZTS-DMSO, were fabricated by spin-coating the MOE-Sn^{4+} and DMSO-Sn^{2+} onto Mo-coated soda-lime glass coated (SLG/Mo), respectively, and then baking. Two kinds of CZTSSe absorbers were produced by selenizing CZTS-MOE and CZTS-DMSO, respectively, and are denoted as CZTSSe-MOE and CZTSSe-DMSO, respectively. By using the CZTSSe-MOE and CZTSSe-DMSO as absorbers, two kinds of CZTSSe solar cells with conventional structure are prepared by using traditional process, and denoted as cell-MOE and cell-DMSO, respectively. The detailed preparation processes are described in Section 4.

Figures 1(a)–1(d) show statistical chart box of PCE, open-circuit voltage (V_{OC}), short-circuit current density (J_{SC}), and fill factor (FF) of cell-MOE and cell-DMSO, which indicates that PCE of cell-MOE is higher than that of cell-DMSO, and the enhancement in PCE of cell-MOE compared with cell-DMSO is due to an increase in its V_{OC} and J_{SC} relative to cell-DMSO. These indicate that the types of solvents and the valence states of Sn exert an influence on photovoltaic performance of CZTSSe solar cells. Figures 1(e)–1(h) show statistical chart box of shunt resistance (R_{Sh}), series resistance (R_S), diode ideality factor (n), and reverse saturation current density (J_0) of cell-MOE and cell-DMSO, respectively, which imply that the increase in PCE of cell-MOE compared with cell-DMSO stems from an increase in R_{Sh} and a decrease in n and J_0 of cell-MOE relative to cell-DMSO.

2.2 Quantitative analysis on effect of change of photovoltaic and electrical parameters induced by change from cell-DMSO to cell-MOE on PCE

In order to understand the mechanism of influence of the types of solvent and valence state of Sn on PCE, CZTSSe solar cells with the highest PCE in the cell-MOE system and the cell-DMSO system are selected as the research devices, respectively. They are denoted as Hcell-MOE and Hcell-DMSO, respectively. Figure 2(a) shows current–voltage (J–V) curves of Hcell-DMSO and Hcell-MOE, from which the photovoltaic parameters of the two devices were extracted, as listed in Table 1. The corresponding electrical parameters, including R_{Sh}, R_S, n, and J_0, as well as photogenerated current density (J_L), were calculated through using the Sites method and the method reported in Refs. [24, 25], as shown in Table 1. It can be seen from Table 1 that the PCE of Hcell-MOE is larger than that of Hcell-DMSO. Using the method reported in Ref. [24], we calculated percentage contribution of the change of V_{OC}, J_{SC}, and FF from Hcell-MOE to Hcell-DMSO to increase in the PCE of Hcell-MOE relative to Hcell-DMSO (donated as η(PCE) (V_{OC}, J_{SC}, FF)), as shown in Fig. 2(b). Figure 2(b) indicates that the increase in the PCE comes mainly from an increase in J_{SC} of Hcell-MOE relative to

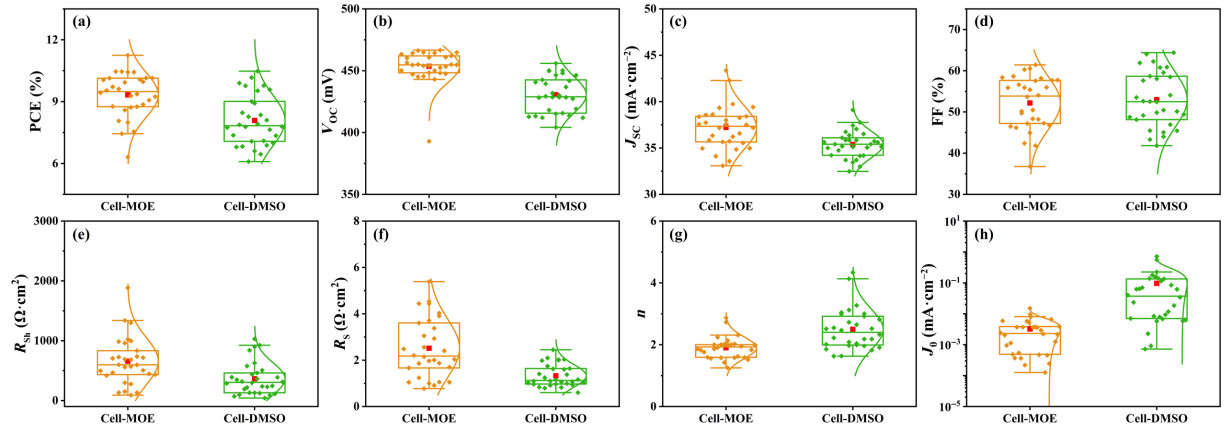

Figure 1 Statistics box charts of (a) PCE, (b) V_{OC}, (c) J_{SC}, (d) FF, (e) R_{Sh}, (f) R_S, (g) n, and (h) J_0 for cell-MOE and cell-DMSO solar cells. In a box plot, the line in the middle represents the median, and the red box represents the mean.

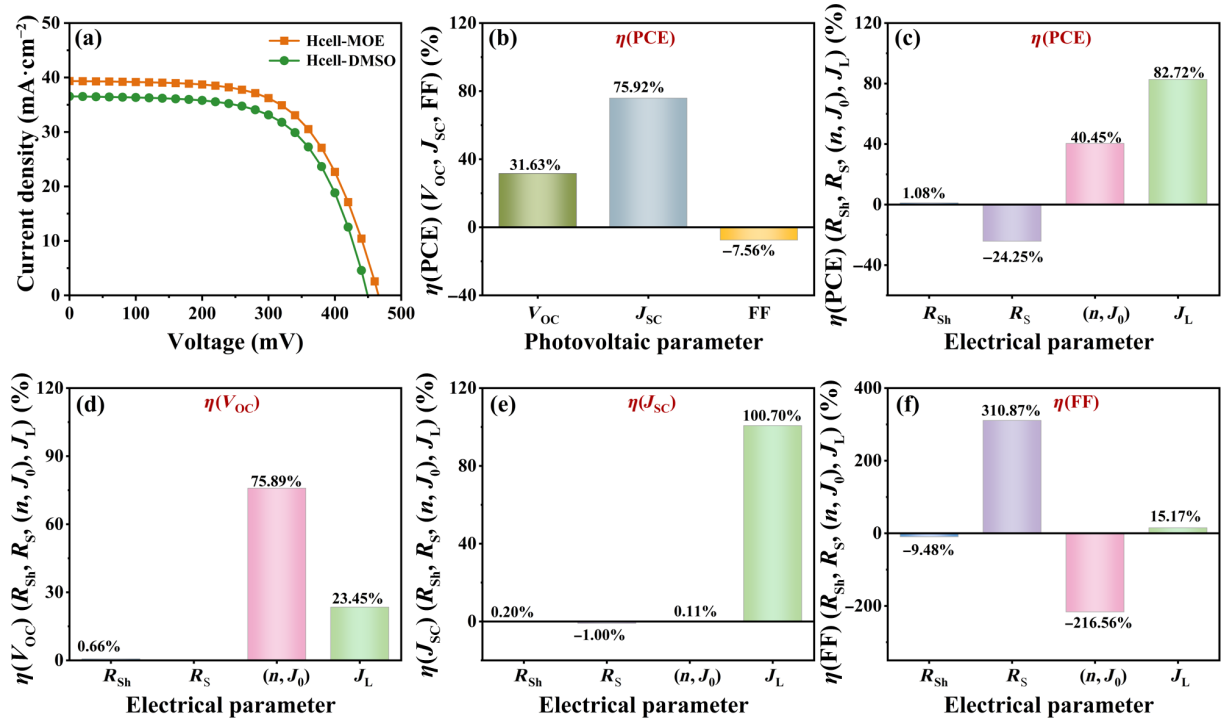

Figure 2 (a) J–V curves of the Hcell-MOE and Hcell-DMSO devices. (b) Column graphs of contribution percentage of changed photovoltaic parameters (V_{OC}, J_{SC}, and FF) to increased PCE for Hcell-DMSO to Hcell-MOE. Column graphs of contribution percentage of changed electric parameters (R_{Sh}, R_S, and (n, J_0)) and J_L to increased (c) PCE, (d) V_{OC}, (e) J_{SC}, and (f) FF for Hcell-DMSO to Hcell-MOE.

Table 1 Photovoltaic parameters (V_{OC}, J_{SC}, FF, and PCE), electric parameters (R_{Sh}, R_S, n, and J_0), and J_L of Hcell-MOE and Hcell-DMSO solar cells

Devices	V_{OC} (mV)	J_{SC} (mA·cm^{-2})	FF (%)	PCE (%)	R_{Sh} (Ω·cm^2)	R_S (Ω·cm^2)	n	J_0 (mA·cm^{-2})	J_L (mA·cm^{-2})
Hcell-MOE	464.77	39.42	61.42	11.25	705.37	1.05	1.86	2.40×10^{-3}	39.42
Hcell-DMSO	450.16	36.51	61.89	10.17	627.60	0.60	2.01	6.27×10^{-3}	36.58

Hcell-DMSO, followed by an increase in its V_{OC}, and that the decrease in its FF has not contributed to the increase in PCE. From Fig. 2(d), the increased V_{OC} results dominantly from decreased (n, J_0), followed by the increase of J_L, while contribution of enhancement of R_{Sh} to the increased V_{OC} is negligible. The increased J_{SC} comes dominantly from enhancement J_L, while contribution of other electrical parameters is ignorable, as shown in Fig. 2(e). The decrease in FF is due mainly to increased R_S, followed by a decrease in J_L. While decreased (n, J_0), and increased R_{Sh} have not contributed to the decrease in, as shown in Fig. 2(f).

It is noted that the results of Figs. 2(b) and 2(c) are different from results reported by Xin and co-workers [19], where the solvents used for preparation of precursor solution of Sn^{2+} and Sn^{4+} are both DMSO. By calculating percentage contribution of changes in photovoltaic parameters and electrical parameters to change in PCE using data given in Ref. [24], it is concluded that the increase in PCE of solar cell prepared by using precursor solution of Sn^{2+} relative to solar cell prepared by using precursor solution of Sn^{4+} is attributed to an enhancement in FF and decreased R_S, as shown in Figs. S2(a)–S2(e) in the Electronic Supplementary Material (ESM).

These indicate that the increase mechanism of PCE is related not only to valence state of Sn but also to types of solvents used.

It is known that PCE is affected through effects of electrical parameters and J_L on photovoltaic parameters, while electrical parameters and J_L are directly related to properties of materials used in solar cells and structure of solar cells. So, to elucidate the mechanism underlying the variation in PCE induced by the differences in solvent types and Sn valence states, it is essential to first identify which among the electrical parameters and J_L are key factors causing the change in PCE. Accordingly, we calculated the percentage contribution of changes of photovoltaic parameters from Hcell-DMSO to Hcell-MOE to variation in PCE of the two devices, and changes of electrical parameters and J_L from Hcell-DMSO to Hcell-MOE to variation in photovoltaic parameters, using data of Table 1 and method reported in Ref. [24], as shown in Figs. 2(c)–2(f). Based on above calculation results, the percentage contribution of changes of electrical parameters and J_L from Hcell-DMSO to Hcell-MOE to variation in PCE were calculated, as shown in Fig. 2(c). From Fig. 2(c), the increased PCE of Hcell-MOE compared to cell-DMSO primarily stems from the increase of its J_L, followed by the decrease of its n and J_0, while the increase of its R_S contributes negatively to PCE. These are confirmed by transient photovoltage (TPV) and transient photocurrent (TPC) spectroscopy measurement results, as shown in Figs. 3(a) and 3(b), which show that Hcell-MOE has higher collection efficiency (η_c) and extraction efficiency (η_e) than Hcell-DMSO, as shown in Fig. 3(a). The higher η_e implies stronger carrier separation capability, that is, larger J_L, and the higher η_c means lower carrier recombination rate, that is, smaller J_0.

2.3 Mechanism of the decreased J_0 for Hcell-DMSO to Hcell-MOE

Now, we first study the mechanism affecting decreases in n and J_0 of Hcell-MOE compared to Hcell-DMSO. It is known that n and J_0 are related to the bandgap (E_g), bulk defects, and surface defects of the absorption layer. In order to investigate the effect of bandgap on J_0, the bandgaps of CZTSSe-MOE and CZTSSe-DMSO are measured by using the measurement of external quantum efficiency (EQE) of cell-MOE and cell-DMSO, and photoluminescence (PL) and ultraviolet absorption spectra (UVAS) of the CZTSSe-MOE and CZTSSe-DMSO, as shown in Figs. 3(c) and 3(d) and Figs. S3(a) and S3(b) in the ESM. From Fig. 3(d) and Figs. S3(a) and S3(b) in the ESM, the E_g of the CZTSSe-MOE and CZTSSe-DMSO are extracted to be 1.063 and 1.102 eV, respectively, from EQE measurement, 0.989 and 1.005 eV, respectively, from PL measurement, and 1.014 and 1.035 eV, respectively, from UVAS measurement. The results obtained from all three measurement technologies demonstrate that the E_g of CZTSSe-DMSO is larger than that of CZTSSe-MOE, which is attributed to the fact that the S/(S + Se) ratio of CZTSSe-DMSO is larger than that of CZTSSe-MOE, as shown in Table S2 in the ESM. According to semiconductor theory, the smaller E_g, the larger J_0 [26, 27]. However, from Table 1, the J_0 of cell-DMSO is not smaller than that of cell-MOE, though the E_g of CZTSSe-DMSO is smaller than that of CZTSSe-MOE. This means that E_g is not dominant factor affecting J_0 in the two devices.

Figure 3(e) shows plots of ln(−ln(1 − EQE)) vs. ($E - E_g$) (E refers to photon energy) of Hcell-MOE and Hcell-DMSO, from which the Urbach energy (E_U) values were extracted to be 44.64 meV for Hcell-MOE and 91.66 meV for Hcell-DMSO. This indicates that the band tail state density of Hcell-MOE is lower than that of Hcell-DMSO, which results in a smaller interfacial recombination rate in Hcell-MOE than in Hcell-DMSO and thus constitutes one of the factors contributing to the lower J_0 of Hcell-MOE relative to Hcell-DMSO [28]. This is confirmed by the Kelvin probe force microscopy (KPFM) measurement results presented in Fig. S4 in the ESM and Fig. 3(f), which show that the contact potential difference (CPD) of CZTSSe-MOE is higher than that of CZTSSe-

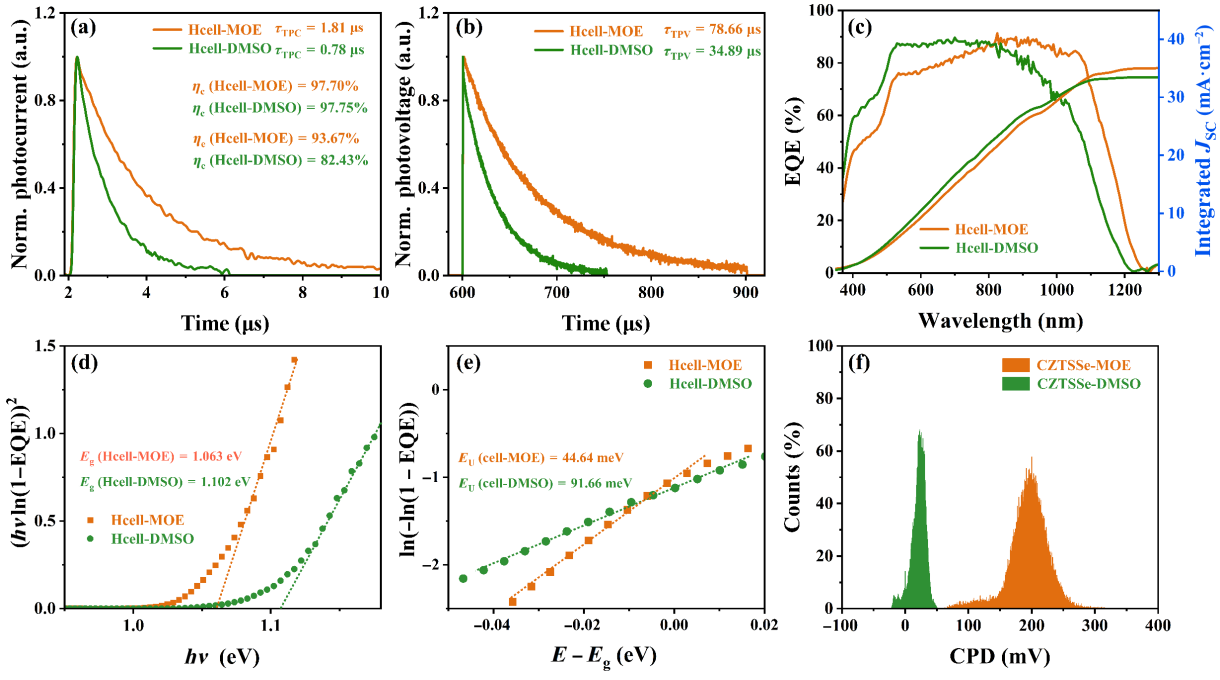

Figure 3 (a) TPC, (b) TPV, (c) EQE spectra and integrated J_{SC} from EQE, (d) ($h\nu$ln(1 − EQE))^2 versus energy plots (here $h\nu$ is the photon energy, where h is the Planck constant and ν is the photon frequency), and (e) ln(−ln(1 − EQE)) versus energy plots of Hcell-MOE and Hcell-DMSO device. (f) The surface CPD distribution of CZTSSe-MOE and CZTSSe-DMSO.

DMSO. This demonstrates that the surface defect density of CZTSSe-MOE is lower than that of CZTSSe-DMSO, which in turn results in a smaller band tail state density of Hcell-MOE compared with Hcell-DMSO [29].

Numerous studies have demonstrated that deep-level defects (such as Sn_{Zn} and $2Cu_{Zn} + Sn_{Zn}$) existing in both the bulk and on the surface of CZTSSe exert a significant influence on J_0 [30, 31]. In order to obtain bulk and interface defects, the capacitance–voltage (*C*–*V*) and drive-level capacitance profiling (DLCP) measurements were performed for Hcell-MOE and Hcell-DMSO. Figure 4(a) shows the plots of the defect densities in the depletion region (N_{CV}) and the bulk of CZTSSe (N_{DLCP}) vs. the distance to the junction. The N_{CV}, N_{DLCP}, and interface defect density (N_{IT}) were extracted from Fig. 4(a) and listed in Table 2. As shown in Table 2, the bulk and interfacial defect densities of Hcell-MOE are lower than the corresponding values of Hcell-DMSO, respectively. Furthermore, the difference in bulk defect density between CZTSSe-MOE and CZTSSe-DMSO (1.27×10^{15} cm^{-3}) is smaller than that in interfacial defect density (7.78×10^{15} cm^{-3}). These results indicate that the reduction in J_0 for Hcell-MOE compared with Hcell-DMSO is attributed to the lower bulk and interfacial defect densities of Hcell-MOE. Furthermore, the reduction in the interfacial defect density of Hcell-MOE relative to Hcell-DMSO is the dominant factor contributing to the decrease in J_0. These are in agreement with J_0 obtained by *J*–*V* measurement (shown in Table 1) and E_g – activation energy (E_a) obtained from temperature-dependent *J*–*V* curves (*J*–*V*–*T*) (shown in Table 2), shown in Fig. 4(b) and Fig. S5 in the ESM. According to literature reports, the smaller the $E_g - E_a$ value, the fewer surface interface composites occur, which is also a key factor contributing to the low J_0 value of Hcell-MOE [32].

To verify the types of surface defects, Raman spectroscopy measurement was performed on the absorber layers of Hcell-MOE and Hcell-DMSO, as shown in Fig. S6 in the ESM. According to literature reported, the vibration peaks at 170, 192, and 235 cm^{-1} belong to the characteristic vibration peaks of CZTSSe [30, 31]. The vibration peaks at 173 and 235 cm^{-1} are related to the density of $[V_{Cu} + Zn_{Cu}]$ and $[2Cu_{Zn} + Sn_{Zn}]$ defect clusters, respectively. The stronger the intensity of the 235 cm^{-1} peak, the higher the density of $[2Cu_{Zn} + Sn_{Zn}]$ defect clusters. As can be seen from Fig. S6 in the ESM, the 235 cm^{-1} peak intensity of the CZTSSe-MOE sample is the weakest. This indicates that the density of $[2Cu_{Zn} + Sn_{Zn}]$ defect clusters on the surface of CZTSSe-MOE is lower than that of CZTSSe-DMSO, suggesting that the reduction of interface defect density in Hcell-MOE is mainly due to the suppression of the formation of deep-level defect clusters $[2Cu_{Zn} + Sn_{Zn}]$.

The X-ray diffraction (XRD) patterns shown in Figs. 4(c) and 4(d) show that both CZTSSe-MOE and CZTSSe-DMSO consist of kesterite CZTSSe and Zn(S, Se) [8, 33]. It can be seen from Fig. 4(e) that the Zn(S, Se) content in the CZTSSe-MOE film is lower than that in the CZTSSe-DMSO film, while the full width at half maximum (FWHM) of the XRD peaks corresponding to the kesterite-structured CZTSSe in the CZTSSe-MOE film is narrower than that in the CZTSSe-DMSO film, as shown in Fig. 4(e). The latter result indicates that the crystalline quality of the kesterite CZTSSe in the CZTSSe-MOE film is superior to that in the CZTSSe-DMSO film, which accounts for the lower defect density of the

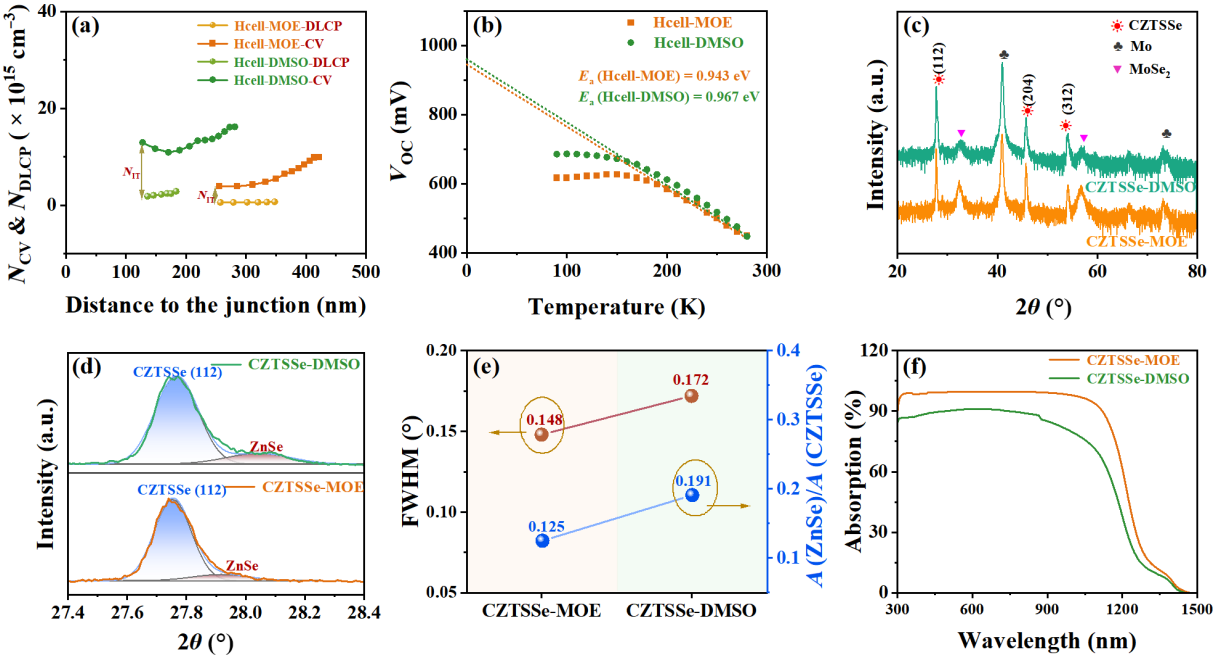

Figure 4 (a) Defect density and depletion region width determined from *C*–*V* measurements (N_{CV}) and DLCP measurements (N_{DLCP}). (b) Plots of V_{OC}–temperature for Hcell-MOE and Hcell-DMSO. (c) XRD patterns. (d) Enlarged XRD patterns of the CZTSSe (112) peaks. (e) The FWHM and the area ratio of ZnSe to CZTSSe. (f) Ultraviolet absorption spectra of CZTSSe-MOE and CZTSSe-DMSO.

Table 2 X_d, N_{CV}, N_{DLCP}, N_{IT}, and E_U of Hcell-MOE and Hcell-DMSO, and E_g of CZTSSe in Hcell-MOE and Hcell-DMSO measured by EQE, PL, and UV–Vis spectrophotometer

Samples	X_d (nm)	N_{CV} (cm^{-3})	N_{DLCP} (cm^{-3})	N_{IT} (cm^{-3})	E_U (meV)	E_g (PL) (eV)	E_g (optical absorption (Abs)) (eV)	E_g (EQE) (eV)	$E_g - E_a$ (eV)
Hcell-MOE	255.57	3.90×10^{15}	5.82×10^{14}	3.32×10^{15}	44.64	0.989	1.014	1.063	0.120
Hcell-DMSO	127.49	1.30×10^{16}	1.85×10^{15}	1.11×10^{16}	91.66	1.005	1.035	1.102	0.135

CZTSSe-MOE film relative to the CZTSSe-DMSO film. The lower Zn(S, Se) content and defect density in CZTSSe-MOE film result in a lower carrier recombination rate in CZTSSe-MOE compared with CZTSSe-DMSO, thereby constituting another key factor contributing to the smaller J_0 of Hcell-MOE relative to Hcell-DMSO.

Scanning electron microscopy (SEM) and XRD characterization results indicate that CZTS-MOE film has the looser structure and smaller grain size than CZTS-DMSO film, as illustrated in Figs. S7(a)–S7(c) in the ESM, which are related to types of solvent and valence state of Sn [19]. During the selenization process, these structural and grain characteristics enhance the reaction degree between Se and CZTS in the MOE-Sn^{4+} film to a greater extent than that in the DMSO-Sn^{2+} film, which in turn promotes the crystal growth of CZTSSe-MOE and ultimately endows CZTSSe-MOE with superior crystallinity compared to CZTSSe-DMSO.

2.4 Mechanism of the increased J_L for Hcell-DMSO to Hcell-MOE

Next, we investigate the mechanism underlying the higher J_L of the Hcell-MOE compared with that of the Hcell-DMSO. It is well known that J_L is mainly affected by the depletion region width (X_d) of p–n heterojunction as well as the absorption coefficient and E_g of absorption layer. From Table 2, the X_d of cell-MOE is wider than that of cell-DMSO. This means that the carrier separation ability of Hcell-MOE is stronger than that of Hcell-DMSO, which is one factor responsible for the higher J_L of Hcell-MOE compared with Hcell-DMSO. Hall measurement and KPFM verify that the wider X_d is due to lower hole concentration of CZTSSe-MOE than that of CZTSSe-DMSO, as shown in Table S3 in the ESM and Fig. 4(f). From Fig. 4(f), the absorption intensity of CZTSSe-MOE is stronger than that of CZTSSe-DMSO in the wavelength range of 400–1200 nm. This indicates that the number of photogenerated electrons and holes in CZTSSe-MOE is greater than that in CZTSSe-DMSO, which contributes to the higher J_L of Hcell-MOE compared with that of Hcell-DMSO. It can thus be deduced that the superior light absorption capability of CZTSSe-MOE over CZTSSe-DMSO constitutes another crucial factor responsible for the higher J_L of Hcell-MOE than that of Hcell-DMSO. From Fig. 3(d) and Table 2, the E_g of kesterite CZTSSe in CZTSSe-MOE is smaller than that in CZTSSe-DMSO. This means that the smaller E_g contributes to an increase in J_L of Hcell-MOE relative to Hcell-DMSO.

2.5 Mechanism of the increased R_S for Hcell-DMSO to Hcell-MOE

Finally, we study the origin of the fact that the R_S of Hcell-MOE (2.93 Ω·cm²) is higher than that of Hcell-DMSO (0.88 Ω·cm²). In this work, R_S is related to the resistivity of the absorption layer and the contact between the absorption layer and the Mo electrode [34]. Hall measurement shows that resistivity of the CZTSSe-MOE is larger than that of CZTSSe-DMSO, as shown in Table S3 in the ESM. XRD and SEM characterization results indicate that a $MoSe_2$ layer forms between CZTSSe and Mo electrode in both Hcell-MOE and Hcell-DMSO, and the thickness of the $MoSe_2$ in Hcell-MOE is thicker than that in Hcell-DMSO, as shown in Fig. 4(c) and Fig. S8 in the ESM. This leads to the contact resistance of CZTSSe and Mo in Hcell-MOE being larger than that in Hcell-DMSO, due to high resistance of $MoSe_2$. The above analysis results indicate that the higher R_S of Hcell-MOE compared with Hcell-DMSO is attributed to the larger resistivity of CZTSSe-MOE and thicker $MoSe_2$ in Hcell-MOE than those in Hcell-DMSO.

3 Conclusions

In summary, two types of CZTSSe solar cells, cell-MOE and cell-DMSO, were prepared by using MOE-Sn^{4+} and DMSO-Sn^{2+} precursor solutions, respectively. It is demonstrated that MOE-Sn^{4+} is more beneficial for the enhancement of PCE than DMSO-Sn^{2+}, resulting in the cell-MOE delivering a higher PCE than the cell-DMSO. The Hcell-MOE cell achieved a maximum PCE of 11.25%, while the Hcell-DMSO cell had a maximum PCE of 10.07%. The higher PCE is mainly attributed to larger J_L of Hcell-MOE over Hcell-DMSO, next is the lower J_0. The larger J_L and lower J_0 stem from the fact that the CZTS-MOE possesses a looser structure and smaller grain size than the CZTSSe-DMSO; this, in turn, confers upon the CZTSSe-MOE superior crystallinity and a lower Zn(S, Se) content relative to the CZTSSe-DMSO. The superior crystallinity and lower Zn(S, Se) content lead to the CZTSSe-MOE exhibiting a lower hole concentration, stronger light absorption capability, and lower deep-level defect density than the CZTSSe-DMSO, which results in the Hcell-MOE having a larger J_L and lower J_0 than the Hcell-DMSO.

4 Experimental

4.1 Materials

CuCl (99.7%, Shanghai Aladdin Biochemical Technology Co., Ltd.), $Zn(CH_3COO)_2$ (99.98%, Shanghai Aladdin Biochemical Technology Co., Ltd.), $SnCl_2{\cdot}2H_2O$ (99.998%, Shanghai Macklin Biochemical Co., Ltd.), $SC(NH_2)_2$ (Shanghai Aladdin Biochemical Technology Co., Ltd.), $ZnCl_2$ (99.8%, Shanghai Aladdin Biochemical Technology Co., Ltd.), $SnCl_4{\cdot}5H_2O$ (99.98%, Shanghai Aladdin Biochemical Technology Co., Ltd.), 2-methoxyethanol (99.8%), and dimethyl sulfoxide (99.9%, Shanghai Aladdin Biochemical Technology Co., Ltd.), $CdSO_4{\cdot}8/3H_2O$ (99.99%, Shanghai Aladdin Biochemical Technology Co., Ltd.), and NH_4OH (analytical reagent (AR), Sinopharm Chemical Reagent Co., Ltd.) were used and without further purification.

4.2 Preparation of precursor solution

The Cu_2ZnSnS_4-DMSO (DMSO-Sn^{2+}) precursor solution of DMSO system was prepared by successively dissolving $SnCl_2{\cdot}2H_2O$ (3.13 mmol·L⁻¹), CuCl (4.75 mmol·L⁻¹), $ZnCl_2$ (3.63 mmol·L⁻¹), and $SC(NH_2)$ (16.79 mmol·L⁻¹) in DMSO (10 mL). The Cu_2ZnSnS_4-MOE (MOE-Sn^{4+}) precursor solution was fabricated by adding CuCl (4.75 mmol·L⁻¹), $SnCl_4{\cdot}5H_2O$ (3.13 mmol·L⁻¹), $Zn(CH_3COO)_2$ (3.63 mmol·L⁻¹), and $SC(NH_2)$ (16.79 mmol·L⁻¹) to 10 mL of MOE solution, followed by heating and stirring at 1000 rpm for 2 h.

4.3 Preparation of precursor films and absorber films

First, we cleaned the purchased back electrode (SLG/Mo, Mo-20K-23) in an ultrasonic cleaner with deionized water and alcohol for 10 min. Then, the precursor solution of MOE-Sn^{4+} or DMSO-Sn^{2+} precursor solution was spin-coated onto the cleaned SLG/Mo surface (the MOE-Sn^{4+} processing was conducted in air, and DMSO-Sn^{2+} processing was performed in an N_2-filled glove box). Subsequently, the wet film coated with the solution was then placed on a heating plate for drying (the MOE-Sn^{4+} system using 280 °C

hot plate for 2 min, and DMSO-Sn^{2+} system using 320 °C hot plate for 3 min). After repeating the spin-coating and drying process 9 times, precursor films with a thickness of approximately 1.2 μm were obtained and named CZTS-MOE and CZTS-DMSO, respectively. The CZTS precursor film was then transferred to a rapid thermal processing (RTP) furnace for selenization annealing. Under a nitrogen flow rate of 100 sccm·min^{-1}, the temperature was raised to 560 °C in 80 s and held for 17 min, and then we allowed it to cool naturally to room temperature to obtain the CZTSSe absorber layer film.

4.4 Fabrication of devices

We deposited the CdS layer on top of the CZTSSe absorber layer. The CdS thin films were obtained by sequentially dissolving $Cd(SO_4)_2{\cdot}8/3H_2O$ (0.0768 g), $NH_4{\cdot}H_2O$ (12.5 mL), and thiourea (0.11 g) in 200 mL of deionized water, followed by chemical bath deposition (CBD) at 65 °C for 16.5 min. Subsequently, the ZnO (50 nm) and indium tin oxide (ITO, 200 nm) layers were magnetron sputter-deposited under an Ar flow of 22 sccm. After that, the top Ag grid pattern gate electrode was deposited by thermal evaporation. Completed devices (glass/Mo/CZTSSe/CdS/ZnO/ITO/Ag) were mechanically patterned into discrete photovoltaic units with a 0.19 cm^2 total device active area. The schematic illustration of device fabrication is shown in Fig. S1 in the ESM.

4.5 Characterization

The crystal structures of CZTSSe films and CZTS precursor films were characterized using an X-ray diffractometer (XRD Rigaku SmartLab SE) equipped with a Cu Kα radiation source. The *J*–*V* curves were measured using a Keithley 2400 Source meter under simulated AM 1.5G solar illumination. The Raman spectrum of the CZTSSe thin film was measured using a Horiba Jobin Yvon high-resolution confocal *in situ* Raman spectrometer (inVia) equipped with a 532 nm laser. The driver-level capacitance profile (DLCP) and *C*–*V* curves of the solar cell device were measured using a Keithley 4200A-SCS system. The surface morphologies of CZTS and cross-section morphologies of CZTSSe films were measured using a scanning electron microscope (SEM Regulus 8100), and the CZTSSe film compositions were characterized through the use of an energy-dispersive X-ray spectroscopy system (EDS, Bruker XFlash) equipped with a voltage of 15 kV. *J*–*V*–*T* characteristic curves were measured over the temperature range from 100 to 280 K using an apparatus equipped with a Model 8200 helium compressor (CTI-Cryogenics, Inc., USA). KPFM scans of grounded bare absorber layers were performed at Bruker Dimension Icon using the new Multi75E-G (BudgetSensors) tip at 0.4 Hz. PL measurements were performed on the device using a HORIBA iHR550 spectrometer equipped with a 532 nm laser. The optical properties of the CZTSSe films were investigated using an ultraviolet–visible (UV–Vis) spectrophotometer (UV-2800(A)).

Electronic Supplementary Material: Supplementary material (PL spectra, KPFM images, Raman spectra, SEM images, and XRD patterns) is available in the online version of this article at https://doi.org/10.26599/NR.2026.94908700.

Data availability

All data needed to support the conclusions in the paper are presented in the manuscript and the Electronic Supplementary Material. Additional data related to this paper may be requested from the corresponding author upon request.

Acknowledgements

This work is supported by the National Natural Science Foundation of China (Nos. 62274077 and 61774075), the Scientific and Technological Development Project of Jilin Province under grant (No. 20240101325JC), and the Fundamental Research Funds for the Central Universities. The instruments used for characterization of properties are supported by the Instrument and Equipment Sharing Platform, College of Physics, Jilin University.

Declaration of competing interest

All the contributing authors report no conflict of interests in this work.

Author contribution statement

M. G. L.: Conceptualization, data curation, formal analysis, investigation, project administration, validation, visualization, writing – original draft, writing – review & editing. B. Y.: Conceptualization, data curation, formal analysis, funding acquisition, investigation, validation, visualization, writing – original draft, writing – review & editing. Y. F. L., Z. H. D., S. L., and H. M. L.: Data curation, formal analysis, investigation, writing – original draft. N. D. and L. Y. S.: Data curation, formal analysis, investigation. All the authors have approved the final manuscript.

Use of AI statement

None.

References

[1] Enkhbat, T.; Enkhbayar, E.; Otgontamir, N.; Sharif, M. H.; Mina, M. S.; Kim, S. Y.; Kim, J. High efficiency CZTSSe solar cells enabled by dual Ag-passivation approach via aqueous solution process. *J. Energy Chem.* **2023**, *77*, 239–246.

[2] Fu, J. J.; Kou, D. X.; Zhou, W. H.; Zhou, Z. J.; Yuan, S. J.; Qi, Y. F.; Wu, S. X. Ag, Ge dual-gradient substitution for low-energy loss and high-efficiency kesterite solar cells. *J. Mater. Chem. A* **2020**, *8*, 22292–22301.

[3] Wang, J. L.; Zhou, J. Z.; Xu, X.; Meng, F. Q.; Xiang, C. X.; Lou, L. C.; Yin, K.; Duan, B. W.; Wu, H. J.; Shi, J. J. et al. Ge bidirectional diffusion to simultaneously engineer back interface and bulk defects in the absorber for efficient CZTSSe solar cells. *Adv. Mater.* **2022**, *34*, 2202858.

[4] Siqin, L.; Yang, C. J.; Guo, J. Y.; Wang, Y. T.; Wang, L.; Li, Y.; Wang, Y. M.; Li, S. Y.; Chen, X. Y.; Luan, H. M. et al. Achieving 11.23% efficiency in CZTSSe solar cells via defect control and interface contact optimization. *Sol. Energy* **2024**, *283*, 112913.

[5] Kim, J.; Jang, J.; Suryawanshi, M. P.; He, M. R.; Heo, J.; Lee, D. S.; Jung, H. R.; Jo, E.; Gang, M. G.; Kim, J. H. et al. Effect of a graphene oxide intermediate layer in $Cu_2ZnSn(S, Se)_4$ solar cells. *J. Mater. Chem. A* **2020**, *8*, 4920–4930.

[6] National Laboratory of the Rockies. *Best Research-Cell Efficiency Chart* [Online]. https://www.nrel.gov/pv/cell-efficiency.html. (accessed Jan 2, 2026).

[7] Keller, J.; Kiselman, K.; Donzel-Gargand, O.; Martin, N. M.; Babucci, M.; Lundberg, O.; Wallin, E.; Stolt, L.; Edoff, M. High-concentration silver alloying and steep back-contact gallium grading enabling

copper indium gallium selenide solar cell with 23.6% efficiency. *Nat. Energy* **2024**, *9*, 467–478.

[8] Li, M. G.; Ma, D.; Yao, B.; Li, Y. F.; Ding, Z. H.; Wang, C. K.; Luan, H. M.; Zhu, C. J. Mechanism of improvement of the power conversion efficiency of $Cu_2ZnSn(S, Se)_4$ solar cells through changing Ag and Cd co-doping form from uniform to non-uniform. *Chem. Eng. J.* **2025**, *515*, 163564.

[9] Zhou, Q.; Sun, Y. L.; Li, H.; Sun, Y. Z.; Zhao, W.; Liang, B. L.; Wang, Y.; Ma, Y. J.; Zhao, L.; Teng, X. Y. et al. Tailoring addition sequence of metal ions in precursor solution drives highly efficient kesterite solar cells. *Adv. Funct. Mater.* **2024**, *34*, 2313301.

[10] Zhao, X. Y.; Li, J. R.; Hu, C. Y.; Qi, Y. F.; Zhou, Z. J.; Kou, D. X.; Zhou, W. H.; Yuan, S. J.; Wu, S. X. Revealing the role of hydrogen in highly efficient Ag-substituted CZTSSe photovoltaic devices: Photoelectric properties modulation and defect passivation. *Nano-Micro Lett.* **2025**, *17*, 84.

[11] Fu, J. J.; Zhang, A. F.; Kou, D. X.; Xiao, Z. W.; Zhou, W. H.; Zhou, Z. J.; Yuan, S. J.; Qi, Y. F.; Zheng, Z.; Wu, S. X. Defect engineering enabling p-type $Mo(S, Se)_2$: TM (TM = V, Nb, Ta) towards high-efficiency kesterite solar cells. *Chem. Eng. J.* **2023**, *457*, 141348.

[12] Zhou, Q.; Hei, J.; Ma, J. H.; Liu, Z. H.; Guo, Z. H.; Sun, Y. L.; Wang, X. Z.; Yan, X. B.; Gao, Z. R.; Teng, X. Y. et al. Controllable *in situ* sodium doping induces uniform nucleation of self-supplied selenium precursor enables large-grain spanning kesterite absorber. *Chem. Eng. J.* **2025**, *523*, 168940.

[13] Wang, Y. F.; Tong, H.; Tao, S. Y.; Dong, L. Z.; Gong, Q. M.; Han, J. S.; Wang, H. P.; Jia, M. Y.; Wu, Z. H.; Zhuang, D. M. et al. Energy band alignment at p–n heterojunction interface in CZTSSe solar cells with novel ZnMgO buffer layer. *Sol. RRL* **2023**, *7*, 2300645.

[14] Wang, Y. F.; Han, J. S.; Tao, S. Y.; Dong, L. Z.; Gong, Q. M.; Wang, H. P.; Jia, M. Y.; Wu, Z. H.; Baranova, M.; Zhou, J. H. et al. Efficiency enhancement of CZTSSe solar cells via thermal treatment of (Zn, Mg)O buffer layers for improving crystallinity and reducing point defects. *Prog. Photovoltaics* **2025**, *33*, 580–590.

[15] Tao, S. Y.; Wang, H. P.; Jia, M. Y.; Han, J. S.; Wu, Z. H.; Zhou, J. H.; Baranova, M.; Zhu, H. W.; Zhao, M.; Zhuang, D. M. Ge-doped CZTSe solar cell efficiency beyond 14% by suppressing recombination. *Adv. Funct. Mater.* **2025**, *35*, 2423251.

[16] Lou, L. C.; Wang, J. L.; Li, Y.; Yin, K.; Xu, X.; Zhang, B. W.; Jiao, M. H.; Chen, S. D.; Guo, T.; Wang, J. C. et al. Multi-interface engineering for all-solution-processed kesterite solar cells. *Joule* **2025**, *9*, 102091.

[17] Wang, J. L.; Meng, F. Q.; Lou, L. C.; Yin, K.; Xu, X.; Jiao, M. H.; Zhang, B. W.; Li, Y. M.; Shi, J. J.; Wu, H. J. et al. Vacancy-enhanced cation ordering via magnesium doping to enable kesterite solar cells with 14.9% certified efficiency. *Nat. Energy* **2025**, *11*, 66–75.

[18] Huang, L. J.; Wei, S.; Pan, D. C. Phase-separation-induced crystal growth for large-grained $Cu_2ZnSn(S, Se)_4$ thin film. *ACS Appl. Mater. Interfaces* **2018**, *10*, 35069–35078.

[19] Gong, Y. C.; Zhang, Y. F.; Zhu, Q.; Zhou, Y. G.; Qiu, R. C.; Niu, C. Y.; Yan, W. B.; Huang, W.; Xin, H. Identifying the origin of the V_{OC} deficit of kesterite solar cells from the two grain growth mechanisms induced by Sn^{2+} and Sn^{4+} precursors in DMSO solution. *Energy Environ. Sci.* **2021**, *14*, 2369–2380.

[20] Zhao, X. Y.; Qi, Y. F.; Li, J. R.; Yuan, S. J.; Zhou, Z. J.; Kou, D. X.; Liu, X. S.; Zhou, W. H.; Meng, Y. N.; Han, L. T. et al. Interfacial engineering of CZTSSe/CdS heterojunctions via hydrogen-modified CdS buffer layers for high-efficiency kesterite solar cells. *Chem. Eng. J.* **2025**, *522*, 168112.

[21] Yao, G.; Wu, Z. C.; Kou, D. X.; Kong, B. Y.; Wei, H.; Shao, Z. P.; Zhou, W. H.; Zhou, Z. J.; Yuan, S. J.; Qi, Y. F. et al. Phase evolution extension of $Cu_2ZnSn(S, Se)_4$ absorber boosting the efficiency of kesterite solar cells to 14.99%. *ACS Energy Lett.* **2025**, *10*, 2761–2769.

[22] Jian, Y.; Zhao, Y. G.; Zhao, J.; Chen, S.; Su, Z. H.; Ma, H. L.; Zhang, X. H.; Liang, G. X. Controllable SnS-vapor-assisted selenization to enhance carrier transport for highly efficient kesterite solar cells. *Adv. Energy Mater.* **2025**, *15*, e04071.

[23] Li, Y. F.; Chen, X. Y.; Wang, R. X.; Zhou, N.; Huang, F.; Zhao, J.; Su, Z. H.; Chen, S.; Liang, G. X. Defect-level trap optimization in $Cu_2ZnSn(S, Se)_4$ photovoltaic materials via Sb^{3+}-doping for over 13% efficiency solar cells. *J. Mater. Chem. A* **2024**, *12*, 10260–10268.

[24] Zhang, J. Y.; Yao, B.; Ding, Z. H.; Li, Y. F.; Wang, T.; Wang, C. K.; Liu, J.; Ma, D.; Zhang, D. X. Efficiency enhancement of $Cu_2ZnSn(S, Se)_4$ solar cells by addition a CuSe intermediate layer between Cu2ZnSn(S, Se)4 and Mo electrode. *J. Alloys Compd.* **2022**, *911*, 165056.

[25] Luan, H. M.; Yao, B.; Li, Y. F.; Liu, R. J.; Ding, Z. H.; Zhang, Z. Z.; Zhao, H. F.; Zhang, L. G. Mechanism of enhanced power conversion efficiency of $Cu_2ZnSn(S, Se)_4$ solar cell by cadmium surface diffusion doping. *J. Alloys Compd.* **2021**, *876*, 160160.

[26] Zhu, Y.; Yao, B.; Ding, Z. H.; Li, Y. F.; Shi, L. Y.; Wang, C. K.; Ma, D.; Li, M. G.; Liu, Y.; Ding, N. et al. Improvement of the performance of $Cu_2ZnSn(S, Se)_4$ solar cells by synergistic effect of nonuniform Ag and In Co-doping. *Sol. Energy* **2025**, *296*, 113575.

[27] Sun, Y. T.; Yao, B.; Jiang, Y. H.; Li, Y. F.; Du, X. B.; Ding, Z. H.; Zhang, J. Y.; Wang, C. K.; Ma, D.; Li, M. G. et al. Improvement of the performance of $Cu_2ZnSn(S, Se)_4$ solar cells by annealing Li-doped Cu_2ZnSnS_4 precursor films in air. *J. Mater. Chem. A* **2025**, *13*, 29504–29515.

[28] Liang, A.; Jian, Y.; Zhao, Y.; Chen, S.; Zhao, J.; Zheng, Z. H.; Luo, J. T.; Ma, H. L.; Zhang, X. H.; Su, Z. H. et al. An effective precursor-solutioned strategy for developing $Cu_2ZnSn(S, Se)_4$ thin film toward high efficiency solar cell. *Adv. Energy Mater.* **2025**, *15*, 2403950.

[29] Mao, Y.; Wang, M. Y.; Huang, Y. Y.; Deng, Y. M.; Chan, W.; Ren, Z. Y.; Gu, E. N.; Sangaraju, S.; Lin, X. Z.; Yang, G. W. 14.13% efficient inkjet-printed kesterite solar cells enabled by selenium compensation through low-temperature selenium post-treatment. *J. Energy Chem.* **2026**, *113*, 872–880.

[30] Zhang, D. X.; Yao, B.; Li, Y. F.; Ding, Z. H.; Wang, C. K.; Zhang, J. Y.; Wang, T.; Ma, D.; Liu, Y. Insight into the role of air-annealing Cu_2ZnSnS_4 precursor films in improving efficiency of $Cu_2ZnSn(S, Se)_4$ solar cells. *J. Alloys Compd.* **2022**, *929*, 167308.

[31] Wang, L. J.; Ban, J. T.; Han, L. T.; Zhou, Z. J.; Zhou, W. H.; Kou, D. X.; Meng, Y. N.; Qi, Y. F.; Yuan, S. J.; Wu, S. X. Defects in kesterite materials towards high-efficiency solar cells: Origin, impact, characterization, and engineering. *J. Mater. Chem. A* **2024**, *12*, 25643–25677.

[32] Yang, W. T.; Ji, Y. X.; Chen, W. X.; Pan, Y. N.; Chen, Z. F.; Wu, S. Y.; Russo, S. P.; Xu, Y.; Smith, T. A.; Chesman, A. et al. The multiple roles of Na ions in highly efficient CZTSSe solar cells. *Small* **2024**, *20*, 2307807.

[33] Chen, X. Y.; Ishaq, M.; Ahmad, N.; Tang, R.; Zheng, Z. H.; Hu, J. G.; Su, Z. H.; Fan, P.; Liang, G. X.; Chen, S. Ag, Ti dual-cation substitution in $Cu_2ZnSn(S, Se)_4$ induced growth promotion and defect suppression for high-efficiency solar cells. *J. Mater. Chem. A* **2022**, *10*, 22791–22802.

[34] Liu, Y.; Wang, C. K.; Ma, D.; Li, M. G.; Sun, Y. T.; Sun, X. F.; Zhu, Y.; Yao, B.; Li, Y. F.; Ding, Z. H. Enhancement of power conversion efficiency of $Cu_2ZnSn(S, Se)_4$ solar cells by pretreating Mo electrode with H_2O_2. *J. Alloys Compd.* **2024**, *983*, 173801.